

# Tight-binding computations of elastic anisotropy of Fe, Xe, and Si under compression

Ronald E. Cohen

*Carnegie Institution of Washington and Center for High Pressure Research, Washington, D.C. 20015*

L. Stixrude\* and Evgeny Wasserman†

*Georgia Institute of Technology, Atlanta, Georgia 30332*

(Received 28 February 1997)

A tight-binding total-energy model parametrized to first-principles linearized augmented plane-wave computations is applied to study elasticity and elastic anisotropy in Fe, Xe, and Si at high pressures. We find that the model works well in reproducing the compression, electronic structure, phase relations, and elasticity in these diverse materials. In Xe, for example, the same parametrization works well over a fivefold compression range from a van der Waals solid to a dense metal. We find that the cubic close-packed structures are all more anisotropic than hexagonal close packed and that at high pressures the elastic anisotropy approaches that of any central force nearest-neighbor model. We find that long-range, nonorthogonal parametrizations are necessary for greatest accuracy. [S0163-1829(97)04738-3]

## INTRODUCTION

In spite of great strides in applying self-consistent electronic structure and total-energy methods within density functional theory (DFT) to real problems in materials ranging from phase diagrams to melting to mapping of phonon potential surfaces, a faster but still reliable method is highly desirable to explore dynamical properties of materials ranging from elasticity to phase transitions, and to simulate large systems. Much progress has been made in developing tight-binding total-energy methods (TBTE) that differ from self-consistent calculations in that a model is developed for the bonding interactions in terms of site centered atomiclike orbitals. Here we further develop and describe a model presented by Cohen, Mehl, and Papaconstantopoulos<sup>1,2</sup> (CMP) that has an accuracy comparable to self-consistent calculations, but at greatly enhanced speed so that complex problems and materials may be studied. Here we show that the method is general for arbitrary elements by giving results and predictions over large ranges of compression for Fe, a transition-metal, Si, which changes from a covalent semiconductor to a close-packed metal with pressure, and Xe, which changes from an atomiclike rare gas to a wide-band metal with pressure.

Elastic properties are important in fields ranging from geophysics<sup>3</sup> to materials research, chemistry, and physics. Elastic anisotropy, characterized, for example, by the differences in sound speed in various directions through different crystals, has not been systematically studied, especially with regard to changes with compression. The strain energy is important in the development of textures and character of phase transitions,<sup>4</sup> in transition temperatures,<sup>5</sup> and for the ground state.<sup>6</sup> We compare our results with those obtained from a simple nearest-neighbor central forces model, where the elastic anisotropy is dependent only on structure and not on the force constants at low pressures.<sup>7</sup>

## I. TIGHT-BINDING TOTAL-ENERGY METHOD

In tight-binding methods, the radial parts of the Hamiltonian and overlap matrices are parametrized. In the two-

center approximation,<sup>8</sup> which is followed here, only integrals between pairs of atoms are included, integrals that involve a potential on one atom and orbitals on two others are neglected, and the potential  $V_{KS}$  is assumed spherically symmetric around each atom. The Hamiltonian and overlap matrices can be written as

$$H_{ij\alpha\beta} = \sum_{\mathbf{l}} \exp[i\mathbf{k}\cdot(\mathbf{R}_{j\mathbf{l}} - \mathbf{R}_i)] h_{ij\alpha\beta\mathbf{l}} \int d\Omega \phi_{i\alpha} \phi_{j\beta}, \quad (1)$$

$$O_{ij\alpha\beta} = \sum_{\mathbf{l}} \exp[i\mathbf{k}\cdot(\mathbf{R}_{j\mathbf{l}} - \mathbf{R}_i)] o_{ij\alpha\beta\mathbf{l}} \int d\Omega \phi_{i\alpha} \phi_{j\beta},$$

where the integrals are the angular integration for orbital  $\alpha$  on atom  $i$  with orbital  $\beta$  on atom  $j\mathbf{l}$  ( $i$  and  $j$  indicate the atom in the primitive cell and  $\mathbf{l}$  is a lattice vector). Angular momentum is quantized along  $z$ , the vector from atom  $j\mathbf{l}$  to atom  $i$ , so that the indices  $\alpha\beta$  are contracted to a total of ten bonding states up to  $d$  states,  $ss\sigma$ ,  $sp\sigma$ ,  $pp\sigma$ ,  $pp\pi$ ,  $sd\sigma$ ,  $pd\sigma$ ,  $pd\pi$ ,  $dd\sigma$ ,  $dd\pi$ , and  $dd\delta$ . For unlike atoms, additional terms  $ps\sigma$ ,  $ds\sigma$ ,  $dp\sigma$ , and  $dp\pi$  must also be included.

In most tight-binding models the parameters  $h$  and  $o$  are fit to results of first-principles band structures<sup>9</sup> or are fit empirically<sup>10</sup> for individual interactions in a given crystal structure. In TBTE methods the total energy  $E$  as a function of the atomic or nuclear positions  $\mathbf{r}$  is represented as a sum of the band-structure term  $E_{bs}$  and additional structure-dependent term(s)  $F$ :

$$E[\mathbf{r}] = E_{bs} + F[\mathbf{r}], \quad (2)$$

which are often represented as a pair potential plus structure-dependent terms that depend, for example, on local coordination.<sup>11</sup>

In most tight-binding models the eigenvalues are obtained by solving the secular equation with  $H$  and  $O$  obtained from the parameters  $h$  and  $o$ . The energy term  $F$  is usually obtained by fitting first-principles equations of state and/or ex-

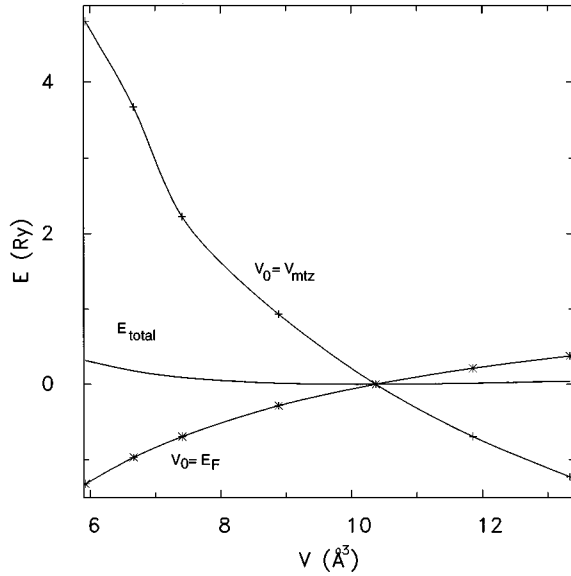


FIG. 1. LAPW band-structure energy,  $E_{bs}$ , obtained for hcp Fe as a function of compression for three different choices of  $V_0$ , the Fermi level  $E_F$ , the LAPW muffin-tin zero  $V_{mtz}$ , or the value needed so that  $E_{bs} = E_{total} + C$  where  $C$  is a constant. Here  $C$  is set so that  $E(P=0) = 0$ .

periment. Although there are tight-binding models that are similar in some ways with the present model<sup>11–20</sup> there are significant differences between the present model and previous nonempirical tight-binding total-energy models: (1) there are no explicit structure-dependent terms; (2) interactions are only distance dependent—there is no division between first and second neighbors, etc.; (3) parameters are fit simultaneously to accurate [linearized augmented plane-wave (LAPW)] electronic structure eigenvalues and total energies (4) over a range of structures and volumes; and (5) there is no explicit pair potential here.

A problem arises when  $E_{bs}$  is fit separately from the function  $F$  [Eq. (2)]. The zero of energy,  $V_0$ , for a band structure is arbitrary, so that  $E_{bs}$  contains an unknown structure-dependent term, which arises from the  $G=0$  term in the Fourier expansion of the Coulomb potential, and is canceled by an identical contribution in  $F[n(\mathbf{r})]$  in self-consistent calculations. To illustrate the severity of the problem, Fig. 1 shows the LAPW band-structure energy  $E_{bs}$  obtained for hcp Fe as a function of compression for different choices of  $V_0$ . If  $V_0$  is chosen to be equal to the Fermi level  $E_F$ ,  $E_{bs}$  is strongly attractive and the function  $F(\mathbf{r})$  must be repulsive. If  $V_0$  is equated with the LAPW muffin-tin zero,  $V_{mtz}$ , the average interstitial potential,  $E_{bs}$  is strongly repulsive and  $F(\mathbf{r})$  must be strongly attractive. We also found it impossible to obtain a pair potential that gave the correct ordering for the energies of nonmagnetic bcc, fcc, and hcp iron with the choice that  $V_0 = E_F$ .

The band-structure energy thus behaves radically differently with compression depending on the choice of  $V_0$ . The large differences are illustrated by the third curve in Fig. 1, which shows the LAPW total energy  $E_{tot}$ . The third curve also represents choosing  $V_0$  such that  $E_{bs} = E_{tot}$ , and this is the most important innovation in the current method. This choice gives a well-defined energy zero that contains no arbitrary constant.

Thus we have for the total energy

$$E_{tot}(\mathbf{r}) = \sum_i \varepsilon'_i f[\varepsilon'_i(\mathbf{k}) - \varepsilon'_F, T], \quad (3)$$

where

$$\varepsilon'_i = \varepsilon_i + \{F[n(\mathbf{r})] + C\}/N_e, \quad (4)$$

and  $\varepsilon_i$  are the band eigenvalues,  $f$  is the Fermi distribution, with  $\varepsilon_F$  chosen to give the correct number of electrons  $N_e$ . The constant  $C$  is chosen for convenience so that the new band-structure energies are not hugely different from the self-consistent ones. (All physical results are completely independent of  $C$ .) This procedure has the added utility of eliminating the structure-dependent potential  $F[\mathbf{r}]$ , usually a pair potential plus other terms, from the problem. Instead, one takes the input band structure and shifts the eigenvalues by Eq. (4) so that

$$E_{tot} = E_{bs} - C. \quad (5)$$

The problem is then reduced to finding a parametrization that accurately reproduces not only the band structure, represented by the  $\varepsilon'_i$ , but also the total energies. Such a parametrization was found and tested for several transition and noble metals.<sup>1</sup> The hopping Hamiltonian  $h$  and overlap  $o$  parameters were parametrized as a function of distance:

$$P_i = (a_i + b_i r) \exp[-c_i^2 r] \xi(r), \quad (6)$$

where  $i$  labels each interactions ( $ss\sigma$ , etc.) and

$$\xi(r) = \{\exp[(r - r_0)/\ell] + 1\}^{-1} \quad (7)$$

is a universal cutoff function to guarantee that interactions vanish smoothly at not too great  $\sigma$ -distance. We generally take  $r_0 = 16.5$  bohrs and  $\ell = 0.5$  bohr. Short-range models are also possible, though less accurate. Here we include  $s$ ,  $p$ , and  $d$  interactions in the two-center approximation, so that there are 60 parameters  $a_i$ ,  $b_i$ , and  $c_i$  for the ten Hamiltonian and ten overlap Slater-Koster parameters for a monoatomic system.

The treatment of the on-site terms is crucial to obtaining good fits to the shifted eigenvalues. Two different methods were used. In the first parametrization, which was presented in Ref. 1 the on-site terms vary as a function of a local “density” around each atom, given by

$$\rho_k = \sum_j \exp[-d_{jk}^2 r] \xi(r), \quad (8)$$

where  $d_{jk}$  depends on atom types  $\tilde{k}$  and  $\tilde{j}$  ( $\tilde{j}$  symbolizes the type of atom  $j$ ). The on-site terms  $D_{\alpha k}$  for  $\alpha = s, p$ , and  $d$  for each atom  $k$  were then fitted to a finite strain polynomial

$$D_{\alpha k} = e_{\alpha \tilde{k}} + g_{\alpha \tilde{k}} \rho_k^{2/3} + h_{\alpha \tilde{k}} \rho_k^{4/3}. \quad (9)$$

This parametrization worked very well for the transition and noble metals studied in Ref. 1 and worked here as well for Xe and Fe. However, for Si it was difficult to obtain an accurate fit using this parametrization. This may be due to the fact that we were attempting to fit a very large range of structures for Si, ranging from 4-coordinated Si in the diamond structure to close-packed metallic structures over a

wide range of compression, whereas the transition metals and Xe were studied primarily for close-packed structures.

We have found a parametrization that works well for Si, and works as well as the previous parametrization for the transition metals and Xe. In this parametrization, we follow Mercer and Chou<sup>12</sup> and Chadi<sup>21</sup> and the on-site terms in the Hamiltonian are given by

$$D_{\alpha m \beta m' k} = q_{\alpha m \beta m' k} + \sum_j I_{\alpha m \beta m' k j} \bar{r}_j(r_{jk}) Y_{\alpha m}(\hat{r}_{jk}) Y_{\beta m'}(\hat{r}_{jk}). \quad (10)$$

This form arises from considering on-site integrals  $\langle \Psi_{ilm} | V_j | \Psi_{il'm'} \rangle$  for interactions of an orbital on atom  $i$  with the same or another orbital on  $i$  with a spherical potential on atom  $j$ . According to Chadi<sup>21</sup> these can be contracted similar to the hopping terms. For example, for  $pp$  on-site terms, Eq. (10) reduces to<sup>12,21</sup>

$$D_{p_z k} = q_{p k} + \sum_j l_{jk}^2(\hat{r}_{jk}) I_{pp\sigma}(r_{jk}) + [1 - l_{jk}^2(\hat{r}_{jk})] I_{pp\pi}(r_{jk}), \quad (11)$$

where  $l_{jk}^2(\hat{r}_{jk}) = z^2/r^2$ , and  $I_{pp\sigma}(\mathbf{r}_{jk})$  and  $I_{pp\pi}(\mathbf{r}_{jk})$  are the distance-dependent terms, represented in our model by  $(s_{i\bar{j}k} + t_{i\bar{j}k} r_{jk}) \exp[-u_{i\bar{j}k}^2 r_{jk}]$ , where  $i$  labels each interaction type ( $ss\sigma$ , etc.).

A full set of such parameters would give forty on-site parameters for a monatomic system. We have found excellent fits for Si, for which we included  $s$ ,  $p$ , and  $d$  interactions (see below) using only the diagonal terms corresponding to  $ss\sigma$ ,  $pp\sigma$ , and  $dd\sigma$ , giving instead twelve on-site parameters. We found that  $pp\sigma$  and  $pp\pi$  were perfectly anticorrelated leading to instabilities in the least-squares fitting, even though our structure set could in principle distinguish between these interactions. We thus removed  $pp\pi$  from the on-site parameter set. So our on-site terms are represented as

$$\begin{aligned} D_s &= q_s + I_{ss\sigma}, \\ D_{p_x} &= q_p + \frac{x^2}{r^2} I_{pp\sigma}, \\ D_{p_y} &= q_p + \frac{y^2}{r^2} I_{pp\sigma}, \\ D_{p_z} &= q_p + \frac{z^2}{r^2} I_{pp\sigma}, \\ D_{d_{xz}} &= q_d + \frac{x^2 z^2}{r^2} I_{dd\sigma}, \\ D_{d_{yz}} &= q_d + \frac{y^2 z^2}{r^2} I_{dd\sigma}, \\ D_{d_{xy}} &= q_d + \frac{x^2 y^2}{r^2} I_{dd\sigma}, \\ D_{d_{(x^2-y^2)}} &= q_d + \frac{(x^2 - y^2)}{r^2} I_{dd\sigma}, \end{aligned}$$

$$D_{d_{(3z^2-r^2)}} = q_d + \frac{3z^2 - r^2}{r^2} I_{dd\sigma}. \quad (12)$$

The two types of on-site treatments are referred to as on-site model I for Eq. (9), and on-site model II for Eq. (12) below.

Since the parameters are correlated and there are multiple minima in the nonlinear least-squares fit of the eigenvalues  $\varepsilon_i'$ , we found it very important to simultaneously fit a set of structures to a single set of parameters, rather than to perform separate fits to different structures and then fit the behavior of the parameters with distance as was done in Ref. 11. We also found it important to fit both the bands and the energies, so that the bands and energies can be individually weighted. The choice of weights was important in obtaining a good fit, and energies were weighted 10–200 times the weighting of an individual band. We fit up to 20 000 input data (eigenvalues and energies) so that the parameters are well constrained. We programmed analytic derivatives so that the Jacobian was obtained analytically; this also increased the stability of the fitting procedure as well as sped up the fitting process by orders of magnitude (see Appendix).

## II. LAPW COMPUTATIONS AND TIGHT-BINDING PARAMETRIZATIONS

Linearized augmented plane-wave<sup>22,23</sup> computations were performed to obtain the band structures (eigenvalues  $\varepsilon_i$ ) and total energies over a wide range of compression and for different crystal structures. For the self-consistent calculations, special  $k$ -point sets were used and were carefully checked for convergence in the total-energy differences between different structures. Extra local orbitals<sup>22</sup> (LAPW+LO) were included in the LAPW computations so that only one energy window could be used and still treat the semicore states accurately, and in order to relax the valence states. Self-consistent total energies and densities were obtained with very dense  $k$ -point meshes ( $16 \times 16 \times 16$  for Fe). Uniform regular  $k$ -point sets were generated on a coarser grid and used in the least-squares fits; we found it important to constrain the eigenvalues at high symmetry points in order to obtain proper ordering of the bands in the tight-binding fits. Different uniform meshes were tested and those used are amply converged. Table I summarizes the nonlinear least-squares fits. States up to 2–5 Ry above  $E_F$  were included in the fits in order to better constrain the individual parameters of the fits. Since the Hamiltonian includes only 9 states per atom for an  $s$ ,  $p$ , and  $d$  state parametrization, and 4 states per atom for an  $s$  and a  $p$  parametrization, it was necessary to discard states that are not in the domain of the Hamiltonian. This was done using the maximum  $l$  character in the muffin tin for each state from the LAPW computations.

For Fe, nonmagnetic computations were performed, so that the ground state is hcp rather than bcc. The present tight-binding model has not yet been generalized to handle magnetic systems. A first-order generalization could be done similar to the tight-binding model of Zhong *et al.*<sup>24</sup> for Fe. Our primary interests are in the behavior of Fe at very high pressures in the non-magnetic fcc and hcp phases, but to understand Fe at low pressures the nonmagnetic model would not be sufficient. We used the generalized gradient approximation<sup>25</sup> (GGA) for Fe since it has been demon-

TABLE I. Summary of self-consistent input and quality of fits. For each structure type is shown the number of structures (e.g., volumes), the maximum number of bands fit, the number of  $k$  points, and the volume range. The number in parentheses is the parametrization identification.

	Fe (8014)	Fe (7)	Xe (62)	Si (8014)	Si (10001)
	Nonorthogonal	Orthogonal	Nonorthogonal	Nonorthogonal	Orthogonal
xc	GGA	GGA	LDA	LDA	LDA
No. of residuals	9743	11377	6798	32841	32841
No. of parameters	73 ( $s,p,d$ )	42 ( $s,p,d$ )	73 ( $s,p,d$ )	72 ( $s,p,d$ )	42 ( $s,p$ )
No. of structures	27	32	15	33	33
Structures:					
fcc	7, 9, 29	12, 10, 29, 30–90	5, 9, 29, 100–500	7, 4, 72, 60–120	7, 4, 72, 60–120
bcc	7, 9, 29	7, 9, 29, 40–90	5, 9, 29, 100–500	7, 4, 72, 60–120	7, 4, 72, 60–120
bct	6, 9, 59	6, 9, 59, 50			
hcp	7, 12, 50	7, 12,50, 40–90	5, 9, 50, 100–500	7, 8, 133, 60–120	7, 8, 133, 60–120
sc				3, 4, 84, 70–120	3, 4, 84, 70–120
Diamond				7, 8, 29, 100–160	7, 8, 29, 100–160
Diamond Raman				2, 8, 65, 110–140	2, 8, 65, 110–140
rms occupied	8	40	21	14	58
Bands (mRyd)					
rms energy mRyd	0.63	0.37	0.17	0.23	1.1

strated to give much more accurate results for Fe than local density approximation (LDA),<sup>3,26,27</sup> including the correct bcc ground state and an accurate phase transition pressure from bcc to hcp in spin polarized calculations.

Figure 2 shows the GGA LAPW and tight-binding band structures of hcp Fe at  $-10$  GPa ( $V=80$  bohrs<sup>3</sup>) and at 530 GPa ( $V=40$  bohrs<sup>3</sup>). The same parameter set does a good job over an extreme range of compression. Figure 3 shows the total energies for bcc, fcc, and hcp Fe as a function of compression and the energy versus tetragonal strain. The band structures and energies are included in the fit, so Figs. 2 and 3 show the quality of the fit.

Figure 4 shows the LAPW and tight-binding band structures for hcp Xe over a fivefold range of compression. The same parameter set works well for the occupied states from low-pressure atomiclike xenon all the way to highly compressed metallic state. Figure 5 shows the metallization behavior of hcp Xe from the tight-binding fit compared with LAPW. Without spin orbit, LDA gives a metallization pressure of  $\sim 90$  GPa, in quite good agreement with experiment. However, with spin orbit this agreement worsens<sup>28</sup> and it is necessary to go beyond LDA to regain an accurate metallization pressure.<sup>28,29</sup> However, LDA gives reasonable energetics (i.e., compression and elasticity) for Xe, and given the importance of spin orbit in Xe for metallization, which we do not include, we have made no attempt to go beyond LDA here.

The tight-binding fit somewhat overestimates the direct gap in Xe; for a detailed study of metallization the bands could be weighted higher in the fit, probably leading to some decrease in the quality of the total energies but improvement in the details of band-gap closure. Figure 6 shows the energy versus volume for bcc, hcp, and fcc xenon. The agreement between the LAPW and tight-binding fit spans 3 orders of magnitude of energy scales, from the 15-eV energy scale over a fivefold compression, to 5-meV structural energy differences at  $P=0$ . Figure 7 shows pressure versus volume compared with experiment. We obtained excellent agreement with the experimental equation of state. We found a phase

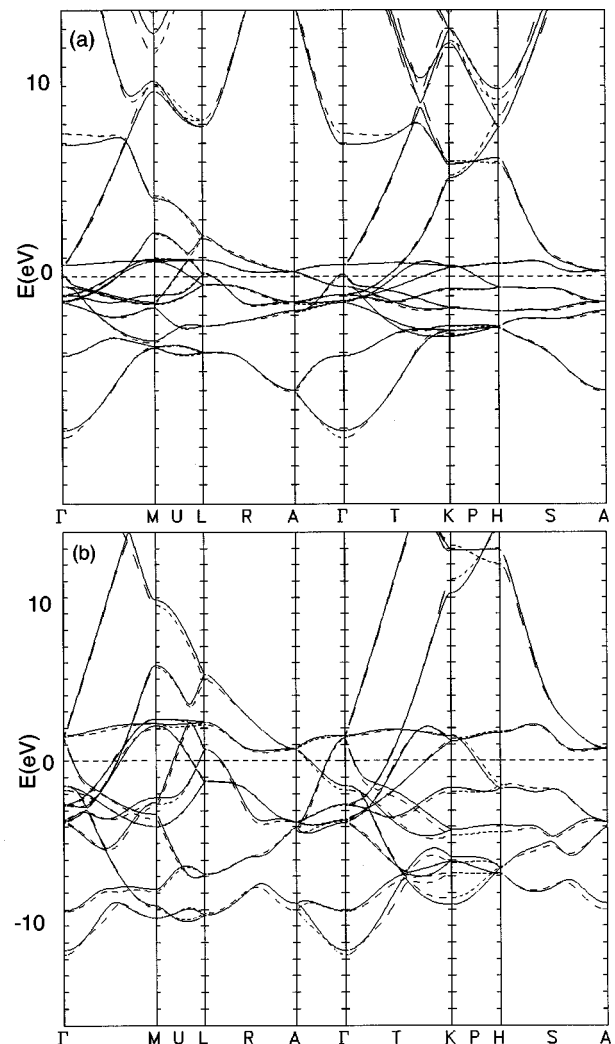


FIG. 2. GGA band structures for hcp Fe at (a)  $-10$  GPa,  $V=80$  bohr<sup>3</sup>/atom, and (b) 530 GPa,  $V=40$  bohr<sup>3</sup>. The solid lines are the LAPW band structure and the dashed are from the nonorthogonal tight-binding fit.

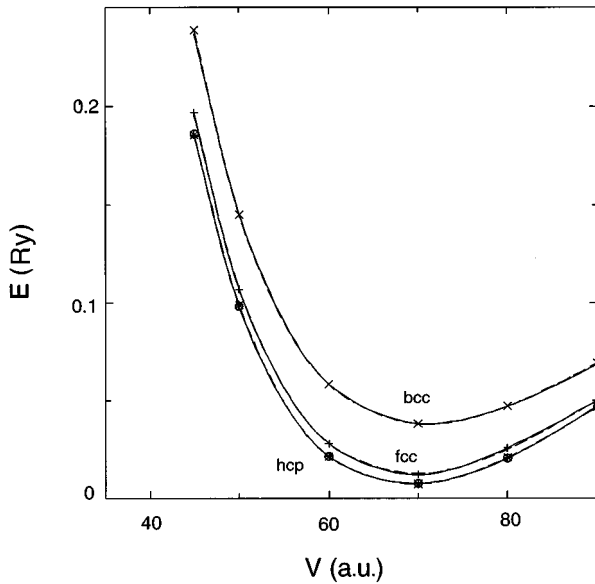


FIG. 3. GGA total energies for nonmagnetic bcc, fcc, and hcp Fe. Solid lines are LAPW; dashed are the nonorthogonal tight-binding fit. The dashed lines are practically superimposed on the solid lines.

transition from hcp to bcc at very high pressures (450 GPa) previously predicted by McMahan.<sup>30</sup>

Good fits for Fe and Xe were obtained using on-site model I [Eq. (9)], but in spite of much effort we were not able to fit Si simultaneously for structures ranging from diamond to close-packed structures fcc and hcp using this parametrization. An accurate *s*, *p*, and *d* fit was obtained using on-site model II [Eq. (10)]. This fit was not as accurate as those obtained for Fe and Xe probably due to the much more extended range of structures and compressions studied for Si. We also found it difficult to obtain an accurate Raman frequency for Si, and had to include the Raman distortion in the fit. Still, getting an accurate Raman frequency as well as accurate phase transition pressures was difficult, and it was necessary to adjust the weights repeatedly until an acceptable fit resulted. Figure 8 shows the band structures for Si for the diamond structure at low pressures for both nonorthogonal and orthogonal fits compared with LAPW. Agreement is not as good as for Fe and Xe due to the higher weighting of the total energies for Si. Figure 9 shows the high-pressure fcc band structures for Si. Although the fit is not as good as for Fe or Xe, it is reasonable and more accurate than previous tight-binding models for Si over such a large range of compression. Better band structures could be obtained if great accuracy in total energies were not required to give the correct phase diagram.

Figure 10 shows the energy versus volume for Si in a number of different structures. The points are the LAPW total energies and the curves are from the tight-binding fit. The agreement with the tight-binding models among the fitted structures is excellent. The nonorthogonal equations of state and phase diagram are in quite good agreement with the self-consistent calculations, including the  $\beta$ -tin and simple hexagonal (SH) structures that were not included in the fit. Although the orthogonal fit gives good equations of state for the fitted structures, it is less accurate with  $\beta$ -tin and SH, and gives a transition from diamond to SH rather than to  $\beta$ -tin.

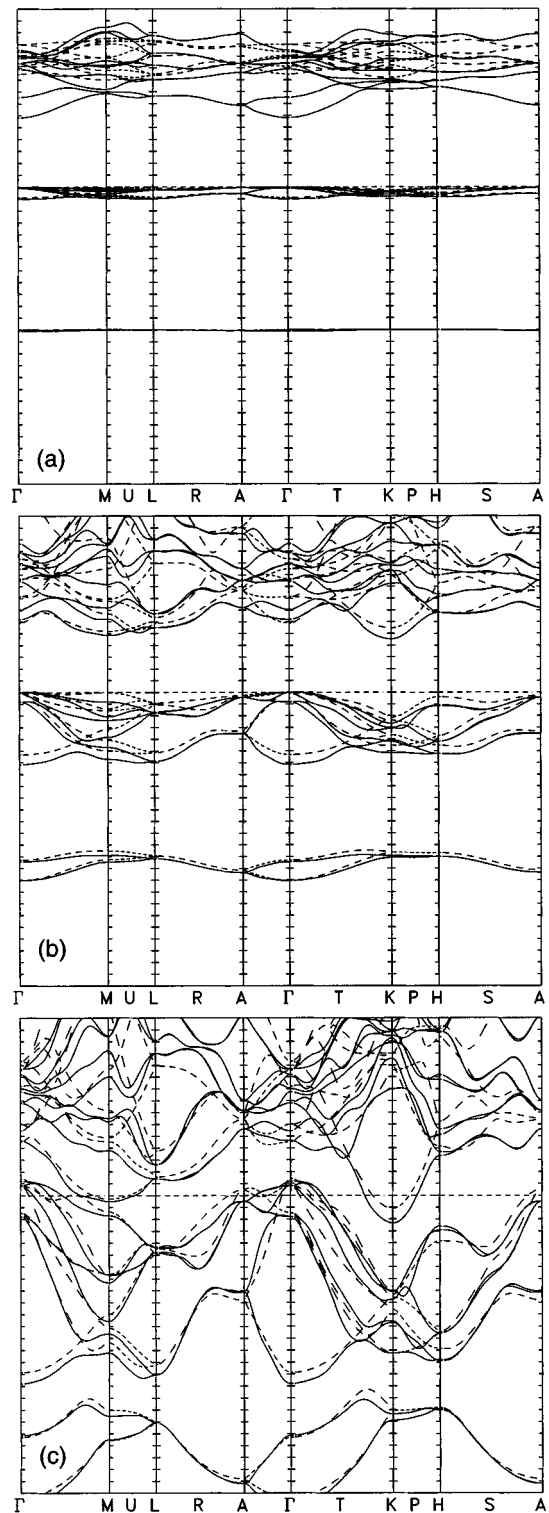


FIG. 4. LDA band structures for hcp Xe at (a) 0 GPa,  $V = 500 \text{ bohr}^3/\text{atom}$ , (b) 20 GPa,  $V = 200 \text{ bohr}^3/\text{atom}$ , and (c) 250 GPa,  $V = 100 \text{ bohr}^3/\text{atom}$ . Solid lines are LAPW band structure; dashed are tight-binding fit.

Figure 11 shows the Raman frequency for Si in the diamond structure as a function of compression compared with experiment. The frequency, which was constrained in the fit by two points, is in excellent agreement with experiment. Again, the nonorthogonal fit is more accurate than the orthogonal one. Table II summarizes the transition pressures obtained for Si.

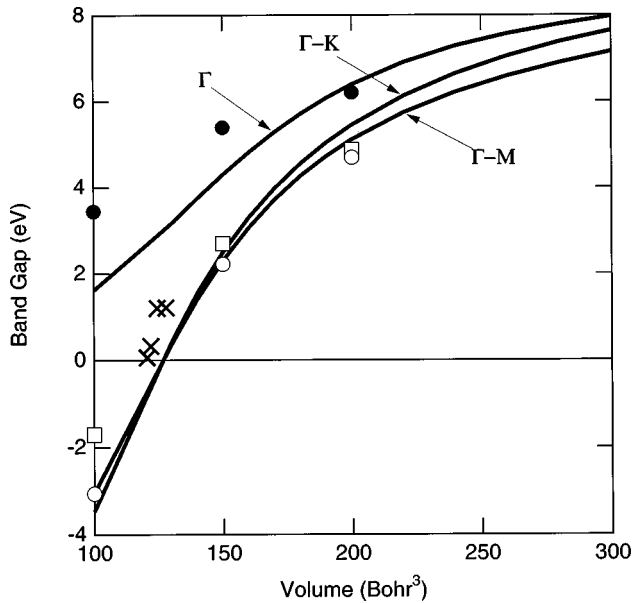


FIG. 5. Band gap vs volume in Xe. Lines are from tight-binding fit; labels refer to the direct gap at zone center ( $\Gamma$ ), and indirect gaps  $K_2-\Gamma_2^-$  and  $M_1^+-\Gamma_2^-$ . Crosses are experimental results (Refs. 39 and 40). Other symbols are LAPW results: direct gap ( $\bullet$ ),  $\Gamma-K$  ( $\circ$ ), and  $\Gamma-M$  ( $\square$ ).

The resulting Si parametrization seems to have the best behavior of any Si parametrization to date over a wide compression range, in that the same parameters accurately reproduce properties of tetrahedrally coordinated diamond and close-packed structures fcc and hcp. Other models for Si that behaved well for diamond are less accurate for the close-packed structures.<sup>11,15,17,19</sup> Also, other models require explicit structure-dependent terms or pair potentials that are absent in the present treatment. One of the best tight-binding models for the energetics of Si, a third-neighbor orthogonal  $s$  and  $p$  model,<sup>31</sup> fit only energetic properties (including empirical data) and not band structures. The predicted phase

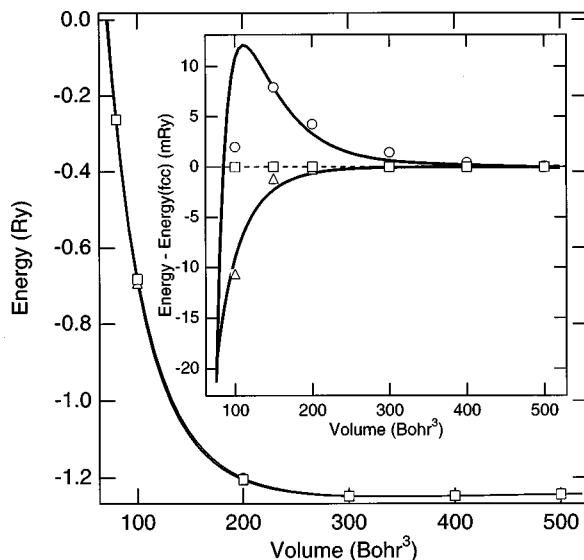


FIG. 6. LDA total energy of bcc, fcc, and hcp phases of Xe. Tight-binding results (solid lines) are compared with LAPW calculations (symbols): bcc ( $\circ$ ), fcc ( $\square$ ), hcp ( $\triangle$ ).

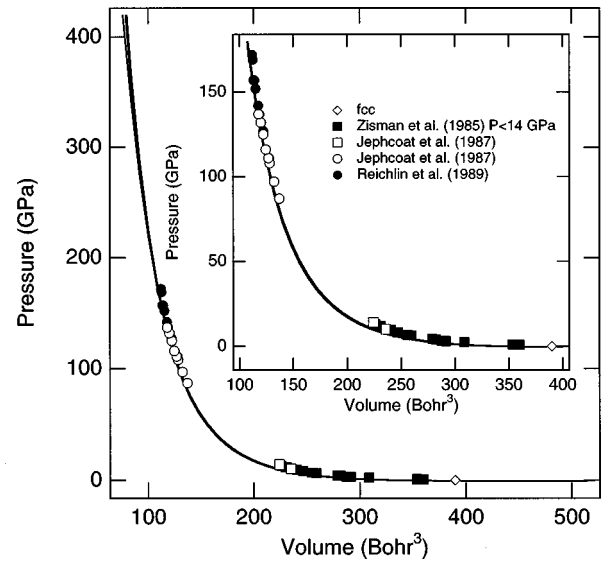


FIG. 7. Pressure vs volume for Xe from the tight-binding model (solid lines) compared with experiment (Refs. 41–43) (fcc: diamond; hcp: other symbols). The theoretical curves are nearly coincident for fcc, hcp, and bcc phases, except at the highest pressures where bcc becomes slightly denser than fcc and hcp.

diagram of Ref. 31, although encouraging, shows major problems such as a large difference in the zero pressure volume for bcc and fcc compared with LDA computations.<sup>32</sup> The authors also pointed out that their band structures, which were not fit, were not accurate. Here we have found a non-orthogonal  $s$ ,  $p$ , and  $d$  model that works well for the band structure and total energies of close-packed and open structures.

We have demonstrated that this tight-binding model is general, and works for transition and noble metals, a rare gas, and a semiconductor, over very large ranges of compression and structure. We now proceed to obtain results not constrained directly in the fits, and study the elasticity and elastic anisotropy of Fe, Xe, and Si.

### III. ELASTICITY

#### A. Elastic constants

Before considering elasticity *per se* we consider  $c/a$  in hcp versus pressure for Fe, Si, and Xe (Fig. 12). We find that the  $c/a$  ratios of Xe and Fe are smaller than the ideal value ( $\sqrt{8/3}$ ) while that of Si is greater. The  $c/a$  ratio of Fe and Si increases slightly with pressure (by 0.02 between 0 and 100 GPa), while that of Xe decreases by a similar amount. Only ideal hcp structures were included in the fits, and predictions for  $c/a$  and the elastic constant  $C_s$  that correspond to  $c/a$  strains agree well with LAPW computations not included in the fit (Fig. 13). This is evidence that the TBTE model is predictive and not simply an interpolation tool.

We obtained the elastic constants as a function of volume for various phases of Fe, Xe, and Si by straining the lattice and allowing the symmetry allowed internal coordinates to relax. In other words, the total energy was minimized with respect to the atomic positions for each increment of strain. The total energy was calculated in the strained lattice for several values of the magnitude of the strain,  $\delta$ . The new

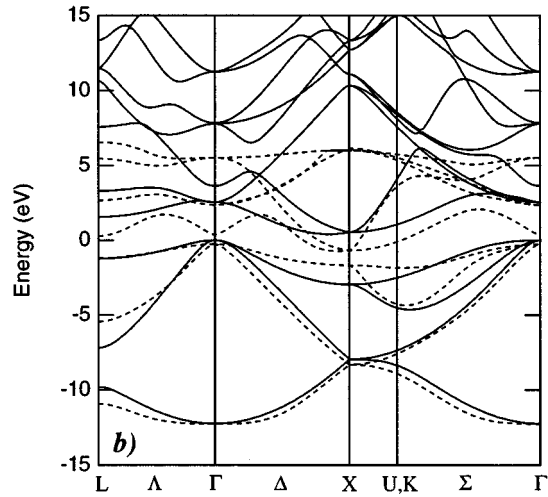
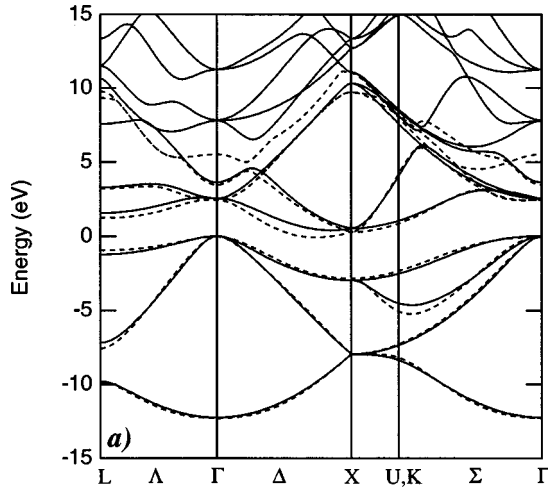


FIG. 8. Band structure of Si in the cubic diamond structure. Solid lines are LAPW band structure, dashed are tight-binding fit. (a) Nonorthogonal model, (b) orthogonal model.

lattice vectors  $P'$  are related to the unstrained  $P$  by  $P' = [I + \varepsilon(\delta)]P$ , where  $\varepsilon$  is the strain matrix. Generally 5–6 values of  $\delta$  were chosen, ranging in magnitude from 0 to 0.1. We fit a polynomial to the total energy as a function of  $\delta$ , from which the elastic constant is given by the coefficient of the quadratic term. Very dense  $k$ -point meshes (up to  $24 \times 24 \times 24$   $k$  points in the full Brillouin zone) were used to ensure sufficient convergence of strain energies. All elastic constants were obtained about the equilibrium relaxed structure at a given volume (pressure).

For cubic crystals, the bulk modulus,  $K = (C_{11} + C_{12})/3$  was obtained by differentiating the equation of state. The shear elastic constant,  $C_S = C_{11} - C_{12}$ , was obtained by applying the volume conserving strain

$$\varepsilon = \begin{pmatrix} \delta & 0 & 0 \\ 0 & \delta & 0 \\ 0 & 0 & (1 + \delta)^{-2} - 1 \end{pmatrix}. \quad (13)$$

The value of  $C_S$  is then determined by the variation of the total energy,  $E$ , with respect to magnitude of the strain,  $\delta$ :

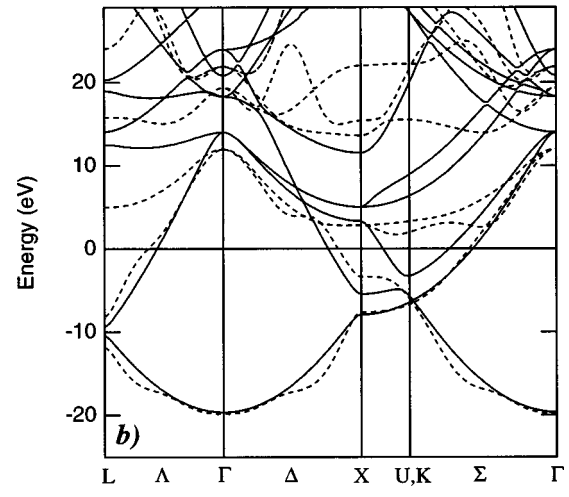
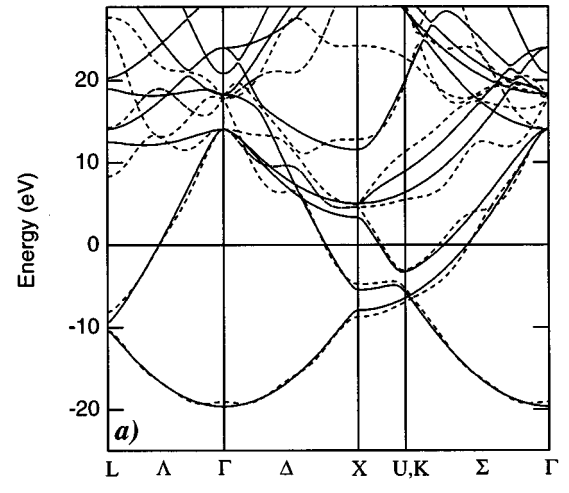


FIG. 9. Band structure of fcc Si. Solid lines are LAPW band structure, dashed are tight-binding fit. (a) Nonorthogonal model, (b) orthogonal model.

$$E(\delta) = E(0) + 3(C_{11} - C_{12})V\delta^2 + O(\delta^3). \quad (14)$$

For the elastic constant  $C_{44}$ , we applied the volume conserving strain

$$\varepsilon = \begin{pmatrix} 0 & \delta & 0 \\ \delta & 0 & 0 \\ 0 & 0 & \delta^2/(1 - \delta^2) \end{pmatrix}, \quad (15)$$

which produces a change in the total energy

$$E(\delta) = E(0) + 2C_{44}V\delta^2 + O[\delta^4]. \quad (16)$$

In the diamond structure, there is one atom located at position  $(x, x, x)$ ; in the unstrained lattice,  $x = 1/8$ . In the diamond lattice strained according to Eq. (15); the equilibrium value of  $x$  differs from  $1/8$ . For each value of  $\delta$ , we redetermined the minimum energy value of  $x$ .

For hexagonal crystals, the bulk modulus yields the combination of elastic constants

$$K = [C_{33}(C_{11} + C_{12}) - 2C_{13}^2]/C_S, \quad (17)$$

where the shear elastic modulus

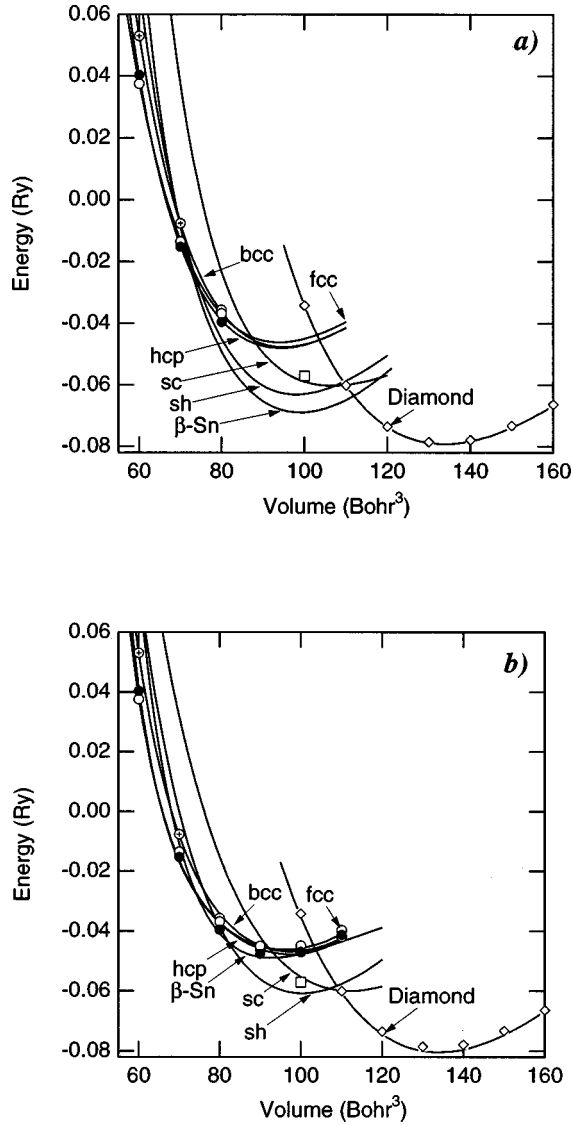


FIG. 10. Total energy of Si in various structures vs volume. Solid lines are tight-binding results, points are LAPW computations: cubic diamond ( $\diamond$ ), simple cubic ( $\square$ ), hcp ( $\bullet$ ), fcc ( $\circ$ ), bcc ( $\oplus$ ). Curves with no points were not constrained in the fits. (a) Nonorthogonal model, (b) orthogonal model.

$$C_S = C_{11} + C_{12} + 2C_{33} - 4C_{13}. \quad (18)$$

The pressure dependence of the  $c/a$  ratio is also related to a combination of elastic constants. The dimensionless quantity  $R$  is defined as

$$R = K \frac{\partial \ln(c/a)}{\partial P} = - \frac{\partial \ln(c/a)}{\partial \ln V} = K(k_a - k_c), \quad (19)$$

where  $k_a$  and  $k_c$  are the linear compressibilities, so that

$$R = (C_{33} - C_{11} - C_{12} + C_{13})/C_S. \quad (20)$$

We determined  $R$  by fitting a polynomial in finite strain to the volume dependence of  $c/a$ . The shear elastic modulus  $C_S$  is determined by applying the strain [Eq. (13)] to the lattice. This yields a variation in total energy

$$E(\delta) = E(0) + C_S V \delta^2 + O[\delta^3]. \quad (21)$$

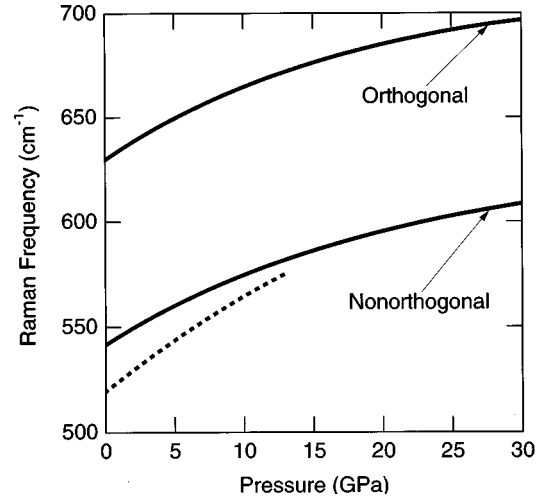


FIG. 11. Raman frequency vs pressure in diamond-structured Si from the tight-binding models (solid lines) and experiment (Ref. 44).

In the combinations of elastic constants  $C_S$ ,  $R$ , and  $K$ ,  $C_{11}$  and  $C_{12}$  always appear as  $C_{11} + C_{12}$ . To determine these two constants individually, we determined the difference between them; in hexagonal crystals,  $2C_{66} = (C_{11} - C_{12})$ . We found that  $C_{66}$  can be efficiently determined by applying a strain to an equivalent orthorhombic lattice, space group  $Cmcm$  with the conventional unit cell  $\vec{a} = (a_{\text{hex}}, 0, 0)$ ,  $\vec{b} = (0, \sqrt{3}a_{\text{hex}}, 0)$ ,  $\vec{c} = (0, 0, c_{\text{hex}})$ , where  $a_{\text{hex}}$  and  $c_{\text{hex}}$  are the

TABLE II. Pressures  $P_t$  of transitions I $\rightarrow$ II in Si and the corresponding volumes of each phase,  $V_t^I$ ,  $V_t^{II}$  (as fractions of the measured equilibrium volume, 135 bohrs<sup>3</sup>) for orthogonal and nonorthogonal tight-binding models, compared with experiment and other theory.

Transition	$P_t$	$V_t^I$	$V_t^{II}$
cd $\rightarrow$ $\beta$ -Sn	Orthogonal	11.7	0.901
	Nonorthogonal	4.5	0.949
	Experiment <sup>a</sup>	12	0.911
	LDA <sup>b</sup>	7.8	0.931
$\beta$ -Sn $\rightarrow$ sh	Orthogonal	25	0.589
	Nonorthogonal	83	0.528
	Experiment <sup>a</sup>	16	0.673
	LDA <sup>b</sup>	10.2	0.690
sh $\rightarrow$ hcp	Orthogonal	28	0.620
	Nonorthogonal	45	0.572
	Experiment <sup>a</sup>	42	0.615
	LDA <sup>b</sup>	37.7	0.594
hcp $\rightarrow$ fcc	Orthogonal	46	0.533
	Nonorthogonal	81	0.479
	Experiment <sup>c</sup>	79	0.481
	LDA <sup>b</sup>	84.3	0.477
	LAPW <sup>d</sup>	78	0.484

<sup>a</sup>Reference 46; <sup>b</sup>Reference 32; <sup>c</sup>Reference 47; <sup>d</sup>This work.



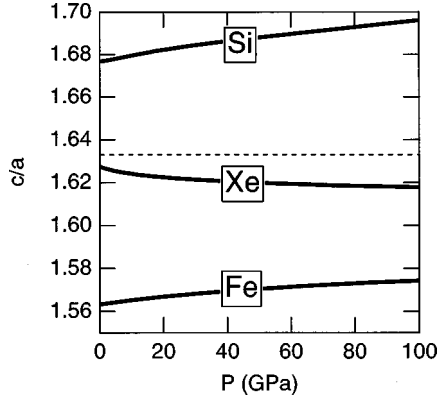


FIG. 12. The  $c/a$  ratios of hcp Xe, Fe, Si as functions of pressure from the nonorthogonal tight-binding models. The dashed line is the ideal  $c/a$  for hexagonal close packing.

hcp lattice parameters. The four atoms in the unit cell are located at Wyckoff position  $4c$  with coordinates  $(0, y, 1/4)$ . The conventional  $c$ -centered unit cell is doubled with respect to the primitive cell. We used the two-atom primitive unit cell in all calculations. We applied the strain matrix

$$\varepsilon = \begin{pmatrix} \delta & 0 & 0 \\ 0 & -\delta & 0 \\ 0 & 0 & \delta^2/(1-\delta^2) \end{pmatrix} \quad (22)$$

to this lattice, leading to a change in the total energy:

$$E(\delta) = E(0) + 2C_{66}V\delta^2 + O[\delta^4]. \quad (23)$$

The atomic coordinate  $y = 2/3$  in the unstrained lattice, but varies when the lattice is subjected to this shear.<sup>33</sup> We redetermined the minimum energy value of  $y$  for each value of strain.

Finally, to determine  $C_{44}$ , we used a monoclinic cell,

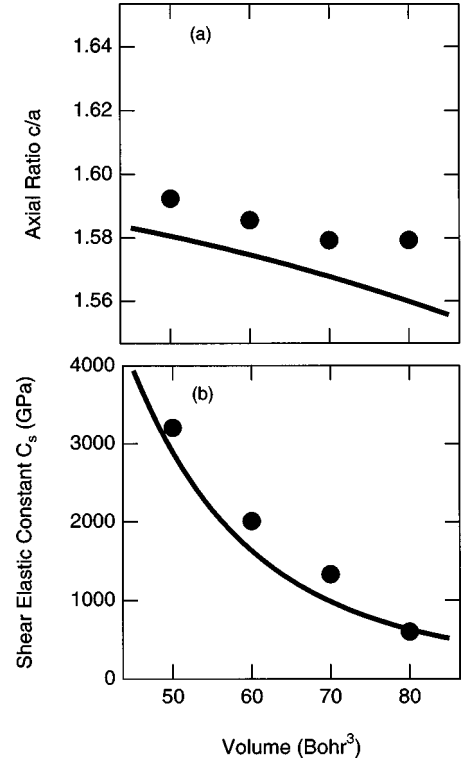


FIG. 13. Comparison of (a) minimum energy  $c/a$  and (b) effective elastic constant  $C_S$  for  $c/a$  strains ( $C_S = C_{11} + C_{12} + 2C_{33} - 4C_{13}$ ) in hcp Fe from LAPW (dots) and the tight-binding model (lines).

space group  $C2/m$ , with lattice vectors  $\vec{a} = (0, \sqrt{3}a_{\text{hex}}, 0)$ ,  $\vec{b} = (a_{\text{hex}}, 0, 0)$ ,  $\vec{c} = (0, 0, c_{\text{hex}})$ . The four atoms in the conventional unit cell are on Wyckoff position  $4i(x, 0, z)$  with  $x = 1/6$  and  $z = 1/4$ . The two-atom primitive cell was used in all calculations. We applied the strain

TABLE III. Elastic constants (GPa) and their pressure derivatives (in parentheses) at zero pressure of the tight-binding model (TB) compared to available experimental data (expt). Zero pressure elastic constants and their pressure derivatives were determined by fitting appropriate finite strain expansions to the tight-binding results (Ref. 48) CD: cubic diamond.

Material	$C_{11}$	$C_{12}$	$C_{44}$	$C_{33}$	$C_{13}$
Fe fcc	448 (6.0)	209 (3.5)	212 (2.2)		
Fe hcp	504 (6.7)	179 (3.2)	159 (1.6)	542 (7.0)	183 (3.0)
Si CD (TB <sup>a</sup> )	183 (0.2)	64 (4.8)	104 (0.2)		
Si CD (TB <sup>b</sup> )	173 (4.1)	58 (3.9)	104 (0.2)		
Si CD (expt <sup>c</sup> )	166 (4.3)	64 (4.2)	80 (0.8)		
Si fcc (TB <sup>a,d</sup> )	58 (7.8)	106 (2.7)	49 (-5.1)		
Si fcc (TB <sup>b,d</sup> )	75 (5.0)	102 (3.5)	6.7 (1.8)		
Si hcp (TB <sup>b,d</sup> )	135 (7.5)	87 (2.7)	-7.9 (3.1)	165 (9.1)	55 (2.6)
Xe fcc (TB)	7.50 (8.5)	5.75 (6.4)	1.71 (3.4)		
Xe fcc (expt <sup>e</sup> )	5.3 (6.0)	2.8 (3.4)	3.0 (3.0)		
Xe hcp (TB)	8.5 (10.1)	5.4 (5.8)	1.1 (1.5)	8.8 (10.5)	5.1 (5.3)

<sup>a</sup>Orthogonal model.

<sup>b</sup>Nonorthogonal model.

<sup>c</sup>Reference 45.

<sup>d</sup>Violates Born stability criteria at low pressure.

<sup>e</sup>Reference 36.

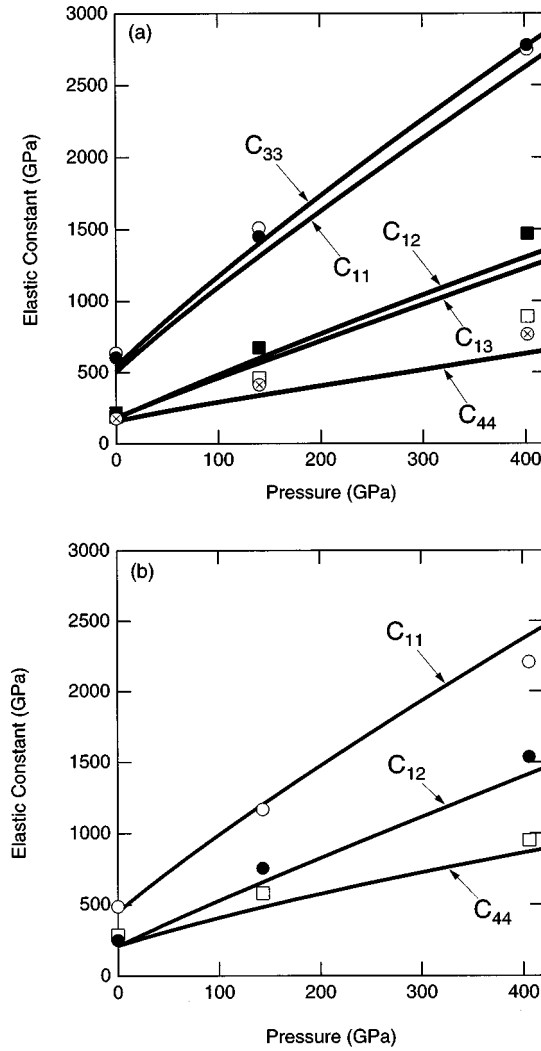


FIG. 14. Predicted elastic constants of (a) hcp and (b) fcc iron vs pressure from the nonorthogonal tight-binding model compared with LMTO results (Ref. 34) (symbols): hcp  $C_{11}$  (●),  $C_{33}$  (○),  $C_{12}$  (■),  $C_{13}$  (□),  $C_{44}$  (⊗); fcc  $C_{11}$  (○),  $C_{12}$  (●),  $C_{44}$  (□).

$$\varepsilon = \begin{pmatrix} 0 & 0 & \delta \\ 0 & \delta^2/(1-\delta^2) & 0 \\ \delta & 0 & 0 \end{pmatrix}, \quad (24)$$

which yields the variation in total energy

$$E(\delta) = E(0) + 2C_{44}\delta^2 + O[\delta^4]. \quad (25)$$

The equilibrium positions of the atoms are unaffected by this strain, and do not need to be redetermined in the strained lattice.<sup>33</sup> The elastic constants of Xe, Fe, and Si at zero pressure are compared in Table III.

The predicted elastic constants for hcp Fe versus pressure are shown in Fig. 14. Our predicted fcc and hcp elastic constants are in generally good agreement with linear muffin-tin orbital (LMTO) results;<sup>34</sup> the rms difference between the two sets of predictions is 70 GPa. The largest difference occurs in  $C_{12}$  of hcp. Whereas we find that  $C_{12}$  and  $C_{13}$  are similar, differing by no more than 6%, the LMTO study finds that  $C_{12}$  is more than 50% smaller than  $C_{13}$  at inner core densities. While the cause of this discrepancy is unclear, we note

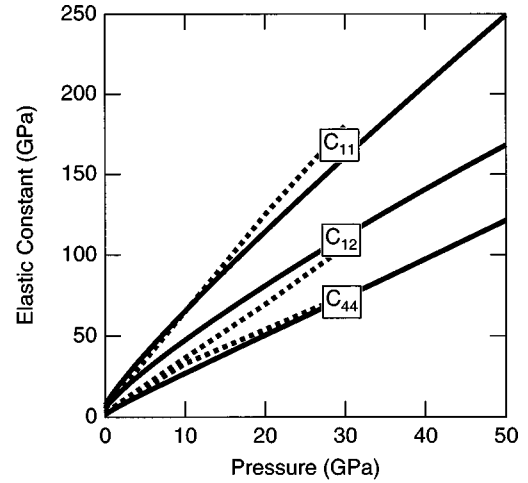


FIG. 15. LDA fcc elastic constants for Xe computed using the tight-binding model (solid lines) and compared with experiment (dashed lines). No strained configurations were used in the fit—only fcc, hcp, and bcc Xe as functions of  $P$ .

that experimental data on other hcp transition metals<sup>35</sup> show  $C_{12} \approx C_{13}$ , consistent with our results. Moreover, the elastic constants in Ref. 34 were obtained using the ideal, rather than the equilibrium value of  $c/a$ . We speculate that this may have biased their results.

Figure 15 shows the elastic constants of fcc Xe as a function of pressure compared with experiment.<sup>36</sup> Agreement is excellent and the elastic constants vary by an order of magnitude over this pressure range. No strained distortions for Xe were included in the fit, so this result indicates clearly that the model is predictive.

Figure 16 shows elastic constants for Si compared with experiment or LAPW for the nonorthogonal parametrization. Both parametrizations give reasonable zero-pressure elastic constants for  $C_{12}$  and  $C_{11}$  but are worse for  $C_{44}$ . The pressure dependencies in the nonorthogonal fit compare quite well with experiment, whereas the orthogonal fit gives an incorrect prediction for the pressure dependence of  $C_{11}$ . It is clear that a nonorthogonal model is needed to give adequate properties for Si over this range of compressions and structures. It is quite probable that a model for diamond structure alone could be much more accurate, especially if the elastic and Raman response were constrained in the fit. However, such a model would not likely give an accurate phase diagram or description of close-packed phases such as the liquid state. Since there are no experimental data for fcc or hcp Si elastic constants we compare with elastic constants derived from LAPW computations and see that agreement is quite good again for the nonorthogonal model. Agreement with the orthogonal model is less good.

## B. Acoustic anisotropy

Acoustic velocities are related to the elastic constants by the Christoffel equation,

$$(C_{jklm}n_k n_l - M\delta_{jm})u_j = 0, \quad (26)$$

where  $C_{jklm}$  is the effective elastic constant relative to a reference state under isotropic pressure,  $\mathbf{n}$  is the wave nor-

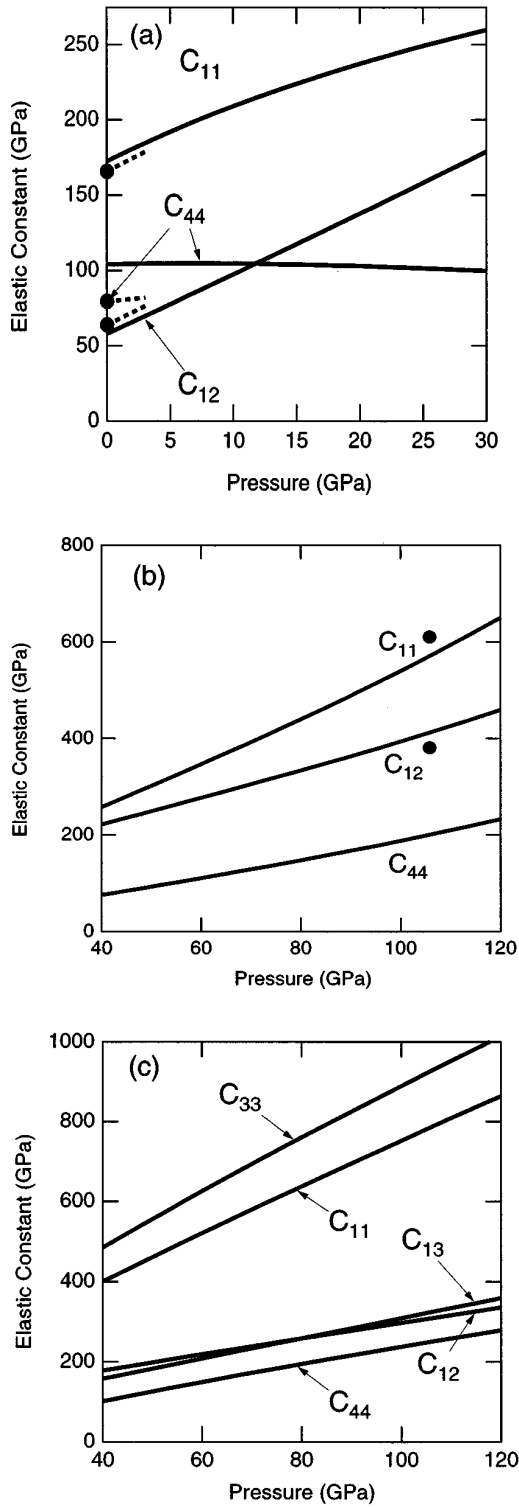


FIG. 16. Elastic constants of Si computed with the nonorthogonal model (solid lines) in various structures: (a) diamond-structured compared with experiment (Ref. 45) (symbols and dashed line) (b) fcc compared with LAPW computations (symbols). The LAPW computations were not used in the fit. (c) hcp.

mal,  $\mathbf{u}$  is the polarization (displacement) vector,  $M = \rho v^2$  is the modulus of propagation,  $\rho$  is the density, and  $v$  is the velocity.

Figure 17 shows the elastic anisotropy calculated using Eq. (26) for fcc and hcp Fe, Xe, and Si. The anisotropy

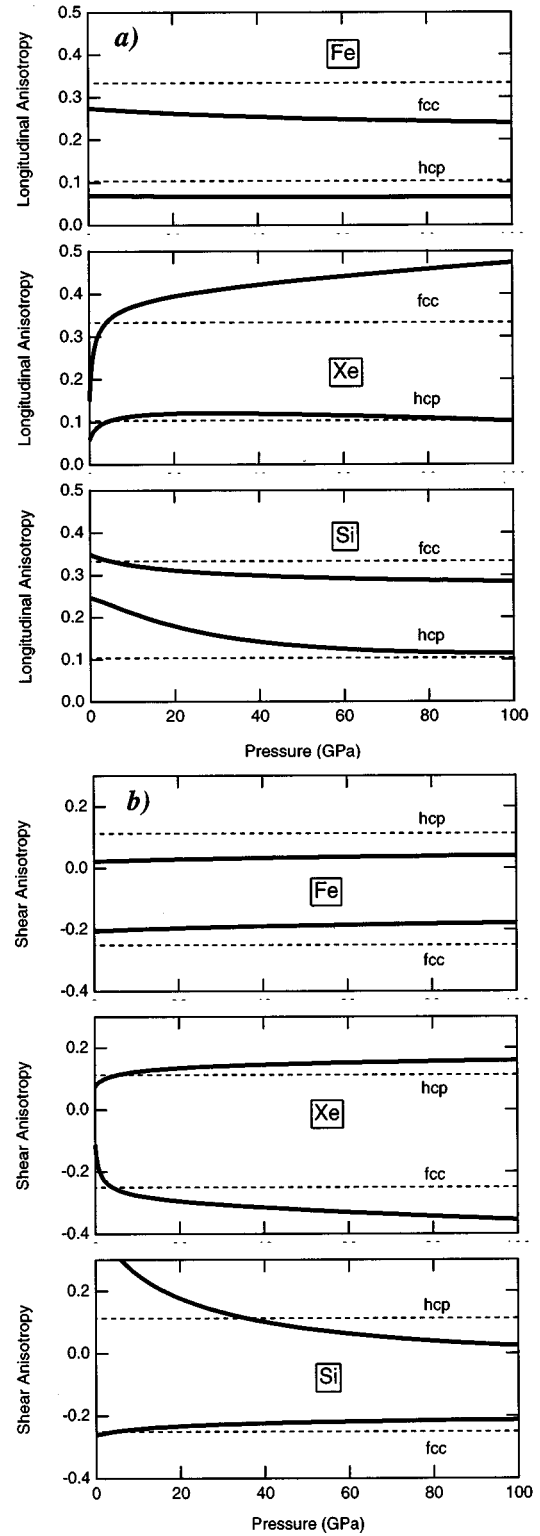


FIG. 17. Amplitude of (a) longitudinal ( $\Delta_p$ ) and (b) shear ( $\Delta_{S1}$ ) anisotropy in Fe, Xe, and Si. For each material, results for fcc and hcp are shown. Solid lines are the tight-binding results, dashed lines represent the CNNF model.

$\Delta_p = (M_p[\mathbf{n}_X] - M_p[100])/C_{11}$ , where  $\mathbf{n}_X$  is the extremal propagation direction other than  $[100]$  and  $p$  is an index that runs over the three types of elastic waves (one longitudinal, two shear). For cubic crystals, the anisotropy is uniquely defined by

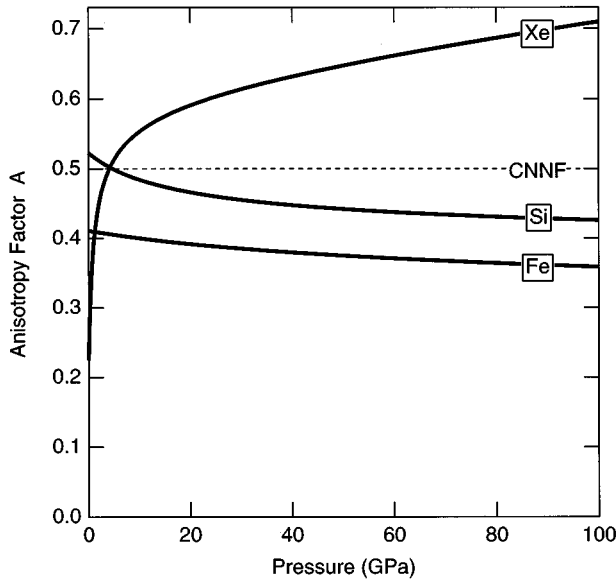


FIG. 18. The quantity  $A = (2C_{44} + C_{12})/C_{11} - 1$ , which defines the anisotropy in the fcc structure. The dashed line is the CNNF result.

$$A = (2C_{44} + C_{12})/C_{11} - 1, \quad (27)$$

which vanishes for an isotropic material. The anisotropies are

$$\Delta_P = \frac{2}{3}A, \quad \Delta_{S1} = -\frac{1}{2}A, \quad \Delta_{S2} = -\frac{3}{8}A, \quad (28)$$

where  $S1$  is polarized in the  $(-110)$  plane and  $S2$  is  $(001)$  polarized. Another way of characterizing anisotropy is to compare it to that of a crystal interacting with central nearest-neighbor forces (CNNF). It has been shown<sup>7</sup> that elastic anisotropy in this case is independent of the interatomic potential to lowest order in  $P/c_{11}$ , which is typically less than 0.1. For an fcc lattice,

$$A_{\text{CNNF}} = \frac{1}{2}(1 - P/C_{11})^{-1}. \quad (29)$$

For hexagonal crystals, the anisotropy is

$$\Delta_P = B, \quad \Delta_{S1} = B/4 - C/2, \quad \Delta_{S2} = A/2, \quad (30)$$

where  $S1$  is  $(010)$  polarized and  $S2$  is  $(001)$  polarized,  $B = C_{33}/C_{11} - 1$  and  $C = (C_{13} + 2C_{44})/C_{11} - 1$ . For an ideal hcp crystal interacting with central near-neighbor forces (neglecting terms of order  $P/C_{11}$ )

$$A_{\text{CNNF}} = -2/29, \quad B_{\text{CNNF}} = 3/29, \quad C_{\text{CNNF}} = -5/29. \quad (31)$$

In spite of the fact that our tight-binding models are not CNNF, we find that at high pressures the elastic anisotropy tends roughly towards the CNNF values. Figure 18 shows the amplitude of the anisotropy as a function of pressure compared with the CNNF. At high pressures Si is closest to the CNNF model in fcc. In fcc Xe is the most noncentral and/or longest ranged at both low and high pressures, which makes sense since nonpairwise overlaps are important, but hcp Xe has quite constant anisotropy. This is a puzzling result since ideal fcc and hcp have the same first- and second-neighbor distances. The anisotropy of Fe does not change

much with pressure in fcc or hcp. In all three materials we find that fcc is more anisotropic than hcp, in agreement with CNNF. Anisotropy at high pressure in Fe is of particular importance in geophysics due to the seismically observed anisotropy in the Earth's inner core. The magnitude and symmetry of the observed anisotropy are very similar to that of hcp Fe, suggesting that the inner core may be a large oriented single crystal of hcp iron<sup>3</sup> or be composed of large oriented crystals. The anisotropy of the Earth's inner core has recently led to the detection of its differential rotation.<sup>38</sup>

#### IV. CONCLUSIONS

We have further developed the tight-binding total-energy model of Ref. 1. A large number of LAPW computations were performed for different crystal structures of Fe, Xe, and Si and the TBTE was parametrized successfully for a large compression range for each. We find that the model works well not only for transition metals such as Fe, but also for the rare gas Xe over a fivefold compression range from Van der Waals insulator to high-density metal, and elemental Si from the open diamond structure to close-packed metallic structures. Using the parametrizations we have computed the elastic constants and anisotropy versus pressure for Fe, Xe, and Si. We find in each case that fcc is more anisotropic than hcp. At high pressures the anisotropy is close to what would be predicted from a nearest-neighbor central force interactions.

#### ACKNOWLEDGMENTS

Much thanks to I. Mazin and J. Mercer, Jr. for helpful discussions. This research was supported by NSF EAR-9305060.

#### APPENDIX: ANALYTICAL EXPRESSION FOR THE FORCES ACTING ON ATOMS AND DERIVATIVES OF THE TOTAL ENERGY WITH RESPECT TO THE PARAMETERS OF THE TBTE FIT

The starting point for this derivation is the expression for the total energy (3). To simplify the notation, the primes denoting shifted eigenvalues are omitted below. As usual, Eq. (3) implies Brillouin zone integration that is performed numerically. The factor of 2 that stems from spin degeneracy of the calculations is not included also. The eigenstates are populated according to the finite-temperature Fermi-Dirac function. The calculations described here were performed with  $k_B T = 5$  mRy. The Fermi level  $\epsilon_F$  is determined by solving the particle conservation equation

$$\sum_i f\left(\frac{\epsilon_i - \epsilon_F}{k_B T}\right) = N_{el}, \quad (A1)$$

where  $N_{el}$  is the number of electrons in the system. Our calculations differ from the previous work (e.g., Ref. 37) in that we do not make an assumption of  $\epsilon_F$  being independent on atomic positions or parameters of the fit. Therefore we are able to perform molecular-dynamics simulations of metallic systems in the NVE (constant number of particles, total energy, and volume) ensemble rather than  $N\mu V$  ensemble. The

dependence of the Fermi level on the parameters of the TBTE fit was found to be significant in most cases.

For clarity, we define here

$$f(X) = \{1 + \exp(X)\}^{-1},$$

which has the derivative

$$\partial f / \partial X = f(f - 1),$$

and the notation

$$f_i = f\left(\frac{\varepsilon_i - \varepsilon_F}{k_B T}\right).$$

In the several equations below,  $a$  denotes either a component of the radius vector of an atom or a fit parameter. The difference between these two cases will be pointed out later. Differentiation of Eq. (3) with respect to  $a$  yields

$$\frac{\partial E_{\text{tot}}}{\partial a} = \sum_i \left[ \frac{\partial \varepsilon_i}{\partial a} f_i + \varepsilon_i \frac{f_i(f_i - 1)}{k_B T} \left( \frac{\partial \varepsilon_i}{\partial a} - \frac{\partial \varepsilon_F}{\partial a} \right) \right]. \quad (\text{A2})$$

For the case of  $T=0$  (this calculation is useful for a wide-gap insulator, but not for a metal) this expression reduces to

$$\frac{\partial E_{\text{tot}}}{\partial a} = \sum_{\text{all } \varepsilon_i < \varepsilon_F} \frac{\partial \varepsilon_i}{\partial a}. \quad (\text{A3})$$

The derivative of the eigenvalue  $\partial \varepsilon_i / \partial a$  is obtained through the Hellmann-Feynman theorem,

$$\frac{\partial \varepsilon_i}{\partial a} = \frac{\left\langle \Psi_i \left| \frac{\partial H}{\partial a} - \varepsilon_i \frac{\partial O}{\partial a} \right| \Psi_i \right\rangle}{\langle \Psi_i | O | \Psi_i \rangle}, \quad (\text{A4})$$

where  $|\Psi_i\rangle$  is the eigenvector corresponding to the eigenvalue  $\varepsilon_i$ . In order to obtain the derivative of the Fermi level with respect to  $a$ , we differentiate Eq. (A1). This yields

$$\sum_i f_i(f_i - 1) \left( \frac{1}{k_B T} \right) \left( \frac{\partial \varepsilon_i}{\partial a} - \frac{\partial \varepsilon_F}{\partial a} \right) = 0. \quad (\text{A5})$$

Solving this equation for  $\partial \varepsilon_F / \partial a$ , one obtains

$$\frac{\partial \varepsilon_F}{\partial a} = \frac{\sum_i f_i(f_i - 1) \frac{\partial \varepsilon_i}{\partial a}}{\sum_i f_i(f_i - 1)}. \quad (\text{A6})$$

Substituting Eq. (A6) and Eq. (A4) into Eq. (A2) solves the problem in principle.

The calculation as outlined here is a computationally intensive task in terms of both the number of floating point operations and the memory usage. Therefore we describe here the ways we found to optimize these calculations. First, the denominator in the Eq. (A4) is equal to 1 since all known generalized eigensolver routines (e.g., DSYEV from LAPACK) normalize the eigenvectors.

In the calculation of forces acting on atoms, the on-site and hopping terms need to be treated separately. Then one adds together the contributions to  $\partial \varepsilon_i / \partial a$  from the on-site and hopping terms. It is important to take advantage of the two-center approximation for the hopping terms of the Hamiltonian and overlap matrix. Formally,  $\partial H_{ij\alpha\beta} / \partial \mathbf{R}_l$  is a

tensor with one extra index. The on-site terms indeed have nonzero derivative with respect to the radius vector of each particle in the system. However, since they are located on the diagonal of the Hamiltonian, the matrix-vector multiplications in Eq. (A4) are reduced to a single sum. Within the framework of the two-center approximation, the hopping matrix elements  $H_{ij\alpha\beta}$  and  $O_{ij\alpha\beta}$  corresponding to atoms  $i$  and  $j$  ( $i, j = 1, \dots, N_{\text{atoms}}$ ,  $i \neq j$ ) and orbitals  $\alpha$  and  $\beta$  are constructed as

$$H_{ij\alpha\beta} = \sum_{\mathbf{n}} \exp[i\mathbf{k} \cdot (\mathbf{R}_j - \mathbf{R}_i + \mathbf{n})] g_{\alpha\beta}(\mathbf{R}_j - \mathbf{R}_i + \mathbf{n}), \quad (\text{A7})$$

where  $\mathbf{R}_j$  is the radius vector of the atom  $j$ ,  $\mathbf{n}$  is the direct lattice vector, and  $g_{\alpha\beta}$  is a function of the separation vector. Therefore,

$$\frac{\partial H_{i\alpha,j\beta}}{\partial \mathbf{R}_l} = \frac{\partial H_{i\alpha,j\beta}}{\partial \mathbf{R}_j} \delta_{jl} + \frac{\partial H_{j\beta,i\alpha}}{\partial \mathbf{R}_i} \delta_{il}, \quad (\text{A8})$$

where  $\delta_{jl}$  is the Kronecker symbol. Taking into consideration that

$$\frac{\partial H_{j\beta,i\alpha}}{\partial \mathbf{R}_i} = - \frac{\partial H_{j\beta,i\alpha}}{\partial \mathbf{R}_j} \quad (\text{A9})$$

and the Hermitian symmetry of the Hamiltonian (and overlap) matrices we arrive at

$$\frac{\partial H_{i\alpha,j\beta}}{\partial \mathbf{R}_l} = \frac{\partial H_{i\alpha,j\beta}}{\partial \mathbf{R}_j} \delta_{jl} - \frac{\partial H_{i\alpha,j\beta}^*}{\partial \mathbf{R}_j} \delta_{il}. \quad (\text{A10})$$

Equations (A7)–(A10) are applicable to the elements of the overlap matrix if one replaces  $H$  by  $O$ . Therefore we construct arrays  $\dot{H}_{i\alpha,j\beta} = \partial H_{i\alpha,j\beta} / \partial \mathbf{R}_j$  and also  $\dot{O}_{i\alpha,j\beta} = \partial O_{i\alpha,j\beta} / \partial \mathbf{R}_j$  (note that there is no extra index  $l = 1, \dots, N_{\text{atoms}}$ ). Denoting for clarity  $M_{i\alpha,j\beta} = \dot{H}_{i\alpha,j\beta} - \varepsilon \dot{O}_{i\alpha,j\beta}$  (the eigenvalue label is suppressed), we can write, using Eq. (A2) and Eq. (A10),

$$\begin{aligned} \frac{\partial \varepsilon}{\partial \mathbf{R}_l} &= \sum_{i\alpha,j\beta} \Psi_{i\alpha}^* \left( \frac{\partial H_{i\alpha,j\beta}}{\partial \mathbf{R}_l} - \varepsilon \frac{\partial O_{i\alpha,j\beta}}{\partial \mathbf{R}_l} \right) \Psi_{j\beta} \\ &= \sum_{i\alpha,j\beta} \Psi_{i\alpha}^* (M_{i\alpha,j\beta} \delta_{jl} - M_{i\alpha,j\beta}^* \delta_{il}) \Psi_{j\beta}. \end{aligned} \quad (\text{A11})$$

Finally, one gets

$$\frac{\partial \varepsilon}{\partial \mathbf{R}_l} = \sum_{i\alpha} \sum_{\beta} \Psi_{i\alpha}^* M_{i\alpha,l\beta} \Psi_{l\beta} - \sum_{j\beta} \sum_{\beta} \Psi_{l\alpha}^* M_{l\alpha,j\beta}^* \Psi_{j\beta}. \quad (\text{A12})$$

Further simplification is possible for the case of the  $\mathbf{k}=0$  calculation. Substituting this result into Eq. (A2), one obtains the gradient of the total energy with respect to the radius vector of an atom. Treating gradients of the hopping and on-site terms separately saves both memory (for each  $k$  point one needs to store only  $3M^2$  values, rather than  $3M^2 N_{\text{atoms}}$  numbers for the perturbation matrices) and computational time. We found from experience that due to memory access considerations, it is best to calculate the quadratic form in Eq. (A4) using matrix-matrix multiplication (so that the re-

sult for all eigenstates is obtained simultaneously) rather than matrix-vector multiplications. It is essential to use vendor-supplied routines for that rather than try to write such a routine in FORTRAN since they are optimized for a particular processor architecture. For example, on IBM RISC/6000 workstations and IBM SP2 we used the ESSL set of routines and found a speedup of a factor of 4.

Calculation of the derivatives of the total energy with respect to the parameters of the TBTE fit differs from the calculation of forces in the following ways. First, a given parameter of the fit [such as  $a_i$ ,  $b_i$  and  $c_i$  in Eq. (6)] influences either elements of the Hamiltonian or the overlap matrix, but not both at the same time. Therefore if  $a$  is a parameter of the Hamiltonian, Eq. (A4) becomes

$$\frac{\partial \varepsilon_i}{\partial a} = \langle \Psi_i | \partial H / \partial a | \Psi_i \rangle. \quad (\text{A13})$$

If it is a parameter of the overlap matrix element,

$$\frac{\partial \varepsilon_i}{\partial a} = -\varepsilon_i \langle \Psi_i | \partial O / \partial a | \Psi_i \rangle. \quad (\text{A14})$$

As the four-index notation suggests, both  $H$  and  $O$  matrices can be considered as block matrices with  $9 \times 9$  blocks (9 is the number of orbitals on each atom we used). Therefore a given parameter of the TBTE fit controls only a submatrix of each  $9 \times 9$  block. Moreover, even though each submatrix (denoted as  $h_{\alpha\beta}$ ) is not symmetric, it has the symmetry properties:

$$h_{\beta\alpha} = p_{\alpha} p_{\beta} h_{\alpha\beta}. \quad (\text{A15})$$

where  $p$  is a vector with integer components  $p = (1, -1, -1, -1, 1, 1, 1, 1, 1)$ . This property of sparseness along with the fact that positions of nonzero elements are known was used extensively to speed up the calculations. Apart from this, the calculation of the derivatives of the eigenvalues and the total energy with respect to the parameters of the TBTE fit is a straightforward but tedious application of Eq. (A6), Eq. (A4), and Eq. (A2).

\*Present address: Dept. Geological Sciences, Univ. Michigan, Ann Arbor, MI 48109-1063.

†Present address: Battelle Pacific Northwest National Laboratory, P.O. Box 999, Richland, WA 99352.

<sup>1</sup>R. E. Cohen, M. J. Mehl, and D. A. Papaconstantopoulos, Phys. Rev. B **50**, 14 694 (1994).

<sup>2</sup>M. J. Mehl and D. A. Papaconstantopoulos, Phys. Rev. B **54**, 4519 (1996).

<sup>3</sup>L. Stixrude and R. E. Cohen, Science **267**, 1972 (1995).

<sup>4</sup>A. M. Bratkovsky, E. Salje, S. C. Marais, and V. Heine, Phase Transit. B **55**, 79 (1995).

<sup>5</sup>W. Zhong, D. Vanderbilt, and K. M. Rabe, Phys. Rev. B **52**, 6301 (1996).

<sup>6</sup>R. E. Cohen, Nature (London) **358**, 136 (1992).

<sup>7</sup>M. Born and K. Huang, *Dynamical Theory of Crystal Lattices* (Clarendon Press, Oxford, 1954).

<sup>8</sup>J. C. Slater and G. F. Koster, Phys. Rev. **94**, 1498 (1954).

<sup>9</sup>D. A. Papaconstantopoulos, *Handbook of the Band Structure of Elemental Solids* (Plenum Press, New York, 1986).

<sup>10</sup>W. A. Harrison, *Electronic Structure and the Properties of Solids: The Physics of the Chemical Bond* (W. H. Freeman and Company, San Francisco, 1980).

<sup>11</sup>J. L. Mercer, Jr. and M. Y. Chou, Phys. Rev. B **47**, 936 (1993).

<sup>12</sup>J. L. Mercer, Jr. and M. Y. Chou, Phys. Rev. B **49**, 8506 (1994).

<sup>13</sup>M. M. Sigalas and D. A. Papaconstantopoulos, Phys. Rev. B **49**, 1574 (1994).

<sup>14</sup>O. L. Alerhand and E. J. Mele, Phys. Rev. B **35**, 5533 (1987).

<sup>15</sup>L. Goodwin, A. J. Skinner, and D. G. Pettifor, Europhys. Lett. **9**, 701 (1989).

<sup>16</sup>F. S. Khan and J. Q. Broughton, Phys. Rev. B **39**, 3688 (1989).

<sup>17</sup>M. Menon and K. R. Subbaswamy, Phys. Rev. B **50**, 11 577 (1994).

<sup>18</sup>D. Tomanek and M. A. Schluter, Phys. Rev. B **36**, 1208 (1987).

<sup>19</sup>C. Z. Wang, C. T. Chan, and K. M. Ho, Phys. Rev. B **45**, 12 227 (1992).

<sup>20</sup>C. H. Xu, C. Z. Wang, C. T. Chan, and K. M. Ho, J. Phys.: Condens. Matter **4**, 604 (1992).

<sup>21</sup>D. J. Chadi, in *Atomistic Simulation of Materials: Beyond Pair*

*Potentials*, edited by V. Vitek and D. J. Srolovitz (Plenum Press, New York, 1989), pp. 309–315.

<sup>22</sup>D. J. Singh, *Planewaves, Pseudopotentials, and the LAPW Method* (Kluwer Academic Publishers, Boston, 1994).

<sup>23</sup>S. H. Wei and H. Krakauer, Phys. Rev. Lett. **55**, 1200 (1985).

<sup>24</sup>W. Zhong, G. Overney, and D. Tomanek, Phys. Rev. B **47**, 95 (1993).

<sup>25</sup>J. P. Perdew, J. A. Chevary, S. H. Vosko, K. A. Jackson, M. R. Pederson, D. J. Singh, and C. Fiolhais, Phys. Rev. B **46**, 6671 (1992).

<sup>26</sup>L. Stixrude and R. E. Cohen, Geophys. Res. Lett. **22**, 125 (1995).

<sup>27</sup>L. Stixrude, R. E. Cohen, and D. Singh, Phys. Rev. B **50**, 6442 (1994).

<sup>28</sup>H. Chacham, X. Zhu, and S. G. Louie, Phys. Rev. B **46**, 6688 (1992).

<sup>29</sup>I. I. Mazin and S. Y. Savrasov, Dokl. Akad. Nauk SSSR **301**, 92 (1988) [Sov. Phys. Dokl. **301**, 92 (1988)].

<sup>30</sup>A. K. McMahan, Phys. Rev. B **33**, 5344 (1986).

<sup>31</sup>T. J. Lenosky, J. D. Kress, I. Kwon, A. F. Voter, B. Edwards, D. F. Richards, S. Yang, and J. B. Adams, Phys. Rev. B **55**, 1528 (1997).

<sup>32</sup>R. J. Needs and A. Mujica, Phys. Rev. B **51**, 9652 (1995).

<sup>33</sup>M. Nastar and F. Willaime, Phys. Rev. B **51**, 6896 (1995).

<sup>34</sup>P. Soderlind, J. A. Moriarty, and J. M. Wills, Phys. Rev. B **53**, 14 063 (1996).

<sup>35</sup>*Smithells Metals Reference Book*, edited by E. A. Brandes (Butterworths, London, 1983).

<sup>36</sup>A. Polian, in *Frontiers of High-Pressure Research*, edited by H. D. Hochheimer and R. D. Eppers (Plenum Press, New York, 1991), pp. 181–192.

<sup>37</sup>S. Goedecker and M. Teter, Phys. Rev. B **51**, 9455 (1995).

<sup>38</sup>X. Song and P. G. Richards, Nature (London) **382**, 221 (1996).

<sup>39</sup>K. A. Goettel, J. H. Eggert, I. F. Silvera, and W. C. Moss, Phys. Rev. Lett. **62**, 665 (1989).

<sup>40</sup>R. Reichlin, K. Brister, A. K. McMahan, M. Ross, S. Martin, Y. K. Vohra, and A. L. Ruoff, Phys. Rev. Lett. **62**, 669 (1989).

<sup>41</sup>A. N. Zisman, I. V. Aleksandrov, and S. M. Stishov, Phys. Rev. B **32**, 484 (1985).

- <sup>42</sup>A. P. Jephcoat, H.-K. Mao, L. W. Finger, D. E. Cox, R. J. Hemley, and C.-S. Zha, *Phys. Rev. Lett.* **59**, 2670 (1987).
- <sup>43</sup>R. Reichlin, K. E. Brister, A. W. McMahan, M. Ross, S. Martin, Y. K. Vohra, and A. L. Ruoff, *Phys. Rev. Lett.* **62**, 669 (1989).
- <sup>44</sup>B. A. Weinstein and G. J. Piermarini, *Phys. Rev. B* **12**, 1172 (1975).
- <sup>45</sup>H. J. McSkimmin and P. Andreatch, *J. Appl. Phys.* **35**, 2161 (1964).
- <sup>46</sup>J. Z. Hu, L. D. Merkle, C. S. Menoni, and I. L. Spain, *Phys. Rev. B* **34**, 4679 (1986).
- <sup>47</sup>S. J. Duclos, Y. K. Vohra, and A. L. Ruoff, *Phys. Rev. B* **41**, 12 021 (1990).
- <sup>48</sup>G. F. Davies, *J. Phys. Chem. Solids* **35**, 1513 (1974).